Design and optimization of functionally-graded triangular lattices for multiple loading conditions

Wang, Junpeng; Westermann, Rüdiger; Gao, Xifeng; Wu, Jun

DOI
10.1016/j.cma.2024.117335

Publication date
2024

Document Version
Final published version

Published in
Computer Methods in Applied Mechanics and Engineering

Citation (APA)
Wang, J., Westermann, R., Gao, X., & Wu, J. (2024). Design and optimization of functionally-graded triangular lattices for multiple loading conditions. *Computer Methods in Applied Mechanics and Engineering*, *432*, Article 117335. https://doi.org/10.1016/j.cma.2024.117335

Computer Methods in Applied Mechanics and Engineering 432 (2024) 117335

Contents lists available at ScienceDirect

Comput. Methods Appl. Mech. Engrg.

journal homepage: www.elsevier.com/locate/cma

Design and optimization of functionally-graded triangular lattices for multiple loading conditions

Junpeng Wang [a], Rüdiger Westermann [a], Xifeng Gao [b], Jun Wu [c,*]

[a] Technical University of Munich, Boltzmannstr. 3, Garching, 85748, Germany
[b] Lightspeed Studios, Bellevue, WA, USA
[c] Delft University of Technology, Landbergstraat 15, Delft, 2628 CE, The Netherlands

GRAPHICAL ABSTRACT

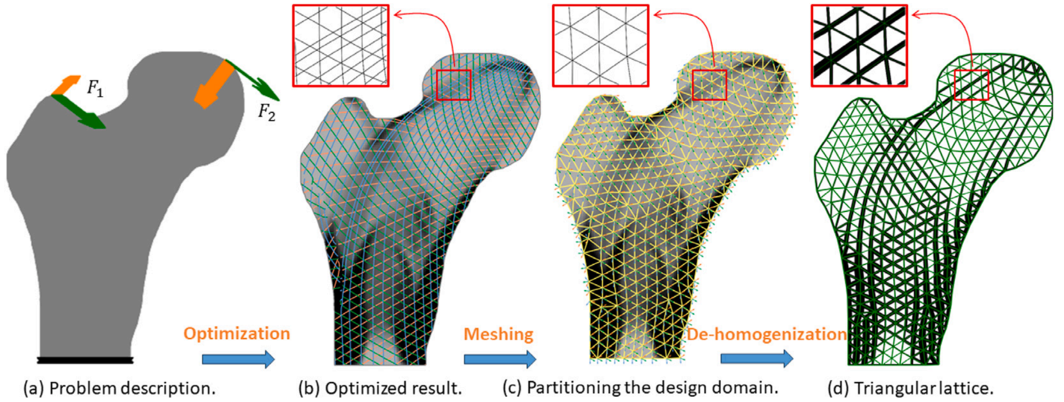

ARTICLE INFO

Keywords:
Topology optimization
De-homogenization
Lattice structures
Multiple loading conditions

ABSTRACT

Aligning lattice infills with the principal stress directions in loaded objects is crucial for improving stiffness. However, this principle only works for a single loading condition, where the stress field in 2D is described by two orthogonal principal stress directions. In this paper, we introduce a novel approach for designing and optimizing triangular lattice structures to accommodate multiple loading conditions, i.e., multiple stress fields need to be considered. Our method comprises two main steps: homogenization-based topology optimization and geometry-based de-homogenization. To ensure geometric regularity of the triangular lattices, we propose a simplified version of the general rank-3 laminate and parameterize the design domain using equilateral triangles with unique edge thickness. During optimization, edge thicknesses and orientations are adjusted based on the homogenized properties of the lattice. Our numerical findings demonstrate that this simplification introduces only a slight decrease in stiffness of less than 5% compared to using the general rank-3 laminate, and results in lattice structures with compelling geometric regularity. For geometry-based de-homogenization, we adopt a

---

* Corresponding author.
E-mail addresses: junpeng.wang@tum.de (J. Wang), westermann@tum.de (R. Westermann), xifgao@tencent.com (X. Gao), j.wu-1@tudelft.nl (J. Wu).

https://doi.org/10.1016/j.cma.2024.117335
Received 8 February 2024; Received in revised form 12 July 2024; Accepted 22 August 2024

field-aligned triangulation approach to generate a globally consistent triangle mesh in which each triangle is oriented according to the optimized orientation field. Our approach for handling multiple loading conditions, akin to de-homogenization techniques for single loading conditions, yields highly detailed, optimized and spatially varying lattice structures. The method is computationally efficient, as simulations and optimizations are conducted at a low-resolution discretization of the design domain. Furthermore, since our approach is geometry-based, obtained structures are encoded into a compact geometric format that facilitates downstream operations such as editing and fabrication.

1. Introduction

Topology optimization and lattice infill are primary strategies for designing lightweight structures. The integration of these two strategies has been a topic of intensive research in the past decade [1]. Topology optimization transforms structural design into an optimization problem of determining where to place material, while lattice infill can be considered as a metamaterial. Topology optimization with lattice infill results in multi-scale structures that are lightweight and robust [2,3]. For an overview of topology optimization methods for designing multi-scale structures, please refer to the recent review article by Wu et al. [4].

For designing load-bearing structures, tailoring the layout of lattice infill based on the stress distribution is key to achieving exceptional structural performance. By aligning the lattice with the principal stress directions, the structural rigidity can be significantly increased [5]. This principle has been well explored and several approaches have been developed [6,7]. Among them, an effective and efficient approach is de-homogenization [8–10]. Firstly, homogenization-based topology optimization is used to specify the optimal lattice infill configuration at each location in the design domain [11]. Secondly, de-homogenization transforms the optimized specifications into a globally consistent structure.

Depending on the representation of the optimized designs, de-homogenization approaches can be classified into *image-based* and *geometry-based*. Image-based approaches represent the structural layout using binary density fields, whereas geometry-based approaches represent this layout using a compact geometric format. For example, a truss-like structure can be represented by a mesh where each edge represents a truss. Geometry-based approaches offer direct control of geometric features, which is beneficial in, e.g., addressing manufacturing constraints [12]. The geometric format also offers a compact parameter space for subsequent editing operations on the optimized structures [10,13]. From a computational perspective, image-based approaches center on computing a fine-grid scalar field, whose gradients are aligned with the orientation of optimized lattice infill from homogenization-based topology optimization, e.g., the projection-based methods [8]. Geometric approaches, in contrast, involve directly computing a set of field-aligned geometric primitives to represent the optimized lattice infill, e.g., the conforming lattice structure [10]. De-homogenization for a single loading condition has been extensively studied in recent years. The projection-based approach proposed by Pantz and Trabelsi [8] was simplified by Groen and Sigmund [9] and further developed by Allaire et al. [14]. It has been extended to design shell-infill structures [15], and to work in 3D [16,17]. Different approaches for the projection have been proposed, from related research fields such as visualization and computer graphics, using stream surfaces [18], convolutional neural networks [19], and phasor noises [20]. Geometric approaches include those based on field-aligned hex-dominant meshing [10] and streamline tracing [13]. The singularity issue in 2D has been investigated respectively in the image- and geometry-based routines by Stutz et al. [21] and Wang et al. [13].

Current de-homogenization approaches consider almost exclusively a single loading condition, i.e., constant external loads. In many engineering applications, however, multiple loading conditions are omnipresent. For instance, in airplane design, the major loads acting on the aircraft wing vary at different stages during the flight, including lift and drag, gravitational forces (particularly when the fuel tanks are fully loaded), propulsion forces from the forward engines, and opposing thrust from thrust reversers. All these loads exert on the airplane during the flight, thus requiring to incorporate them into the structural design and optimization process.

De-homogenization under multiple loading conditions, however, is challenging. Firstly, the optimized metamaterial properties can be realized by different lattice configurations, i.e., the optimal lattice configurations are not uniquely defined. Furthermore, the optimized lattice configuration exhibits severe discontinuities. This further complicates the de-homogenization of a consistent structural layout. An image-based approach addressing these challenges was recently proposed by Jensen et al. [22], by extending the projection approach by Groen et al. [9] from single to multiple loading conditions. The rank-3 laminate was used as the lattice infill for homogenization. It describes a composite material composed of three differently oriented material layers, where each material layer is described by an orientation variable and a width variable. I.e., a rank-3 laminate involves three independent width variables and three orientation variables. The resulting structural designs achieve similar mechanical performance (i.e., stiffness) than those obtained from conventional density-based topology optimization, while the latter incurs a significantly larger computational burden. The image-based projection method inherently requires the integrability of the optimized specifications, making it necessary to ensure the smoothness of the optimized orientation field. This, however, becomes difficult due to the non-uniqueness of the optimal solutions of the homogenization model. In addition, as the three orientation fields are de-homogenized independently, the sub-structures aligning with different orientation fields can come very close to each other, leaving small void regions in the final designs. While this feature does not necessarily impact mechanical performance, it may not be the preferred choice in certain design or manufacturing scenarios due to the increased geometric complexity it introduces. The close-up view in Fig. 1b shows such

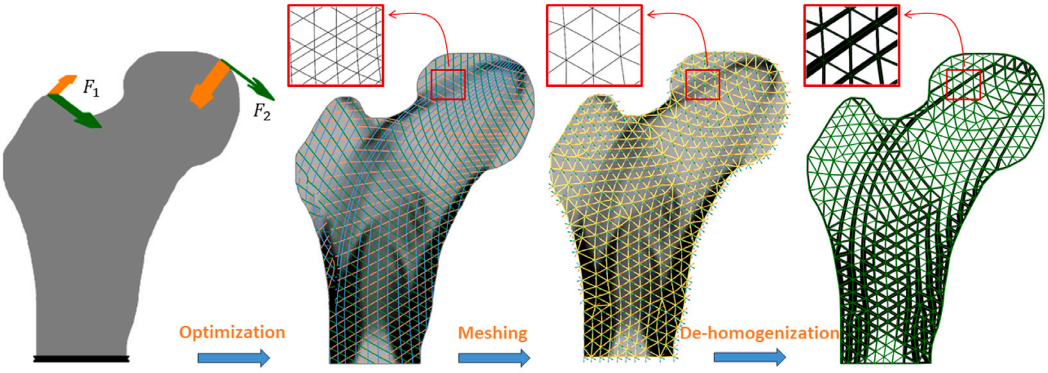

(a) Problem description. (b) Optimized result. (c) Partitioning the design domain. (d) Triangular lattice.

Fig. 1. Method overview. (a) The optimization problem: Two loading conditions F_1 (orange) and F_2 (green) are applied, and the bottom is fixed. (b) The optimized density layout (background) and orientations (streamlines) generated by homogenization-based topology optimization. (c) The triangular parametrization with edges aligned to the tangents of the optimized rank-3 layers. The entire design domain and the optimized density layout are partitioned into sub-domains by this field-aligned mesh. (d) The triangular lattice design obtained via de-homogenization. (For interpretation of the references to colour in this figure legend, the reader is referred to the web version of this article.)

irregular intersections of three orientation fields. In this paper, we present a novel method to generate functionally-graded triangular lattice structures that are resilient to multiple loading conditions. Our method follows the established de-homogenization pipeline, consisting of two steps: (*i*) performing homogenization-based topology optimization to obtain a set of optimized specifications; (*ii*) converting the optimized specifications into a graded triangular lattice structure. Fig. 1 shows an overview of the proposed method.

Our technical contributions are two-fold. Firstly, we propose a simple and effective infill model for multiple loading conditions — triangular lattices. It can be viewed as a simplified version of the general rank-3 laminate. In triangular lattices, the width of each edge is allowed to change independently, creating a large range of attainable metamaterial properties. More importantly, the triangles are rotatable, allowing local alignment of their anisotropy with preferred directions. Secondly, we develop a geometric approach for translating the optimized specifications into a globally conforming triangular lattice structure, whose edges align with the three optimized orientation fields. The edge thicknesses convey the mechanical anisotropy. Our de-homogenization approach is based on field-aligned triangulation [23]. Since it is based on local smoothing operations, it does not require the integrability of the optimized specifications. Thus, a global parametrization can be avoided. In addition, compared to alternative designs exhibiting randomly intersecting substructures, our de-homogenization using equilateral triangles restricts the geometric complexity by carefully placing the intersections. This results in triangular lattices with equal spacing, as shown in the close-up views in Fig. 1c and d.

The remainder of this paper is organized as follows. In Section 2 we first present the triangular lattices by simplifying the general rank-3 laminate, and we introduce the corresponding equation of homogenization-based topology optimization. The construction of de-homogenization is presented in Section 3. In Section 4, we perform numerical experiments and use them to discuss and compare the proposed method. Finally, Section 5 concludes the paper with a summary and an outlook.

2. Topology optimization with triangular lattices

2.1. Triangular lattices

Our triangular infill model is a simplified version of the general rank-3 laminate. Stiffness-optimal structures can be described by a set of spatially varying rank-N laminates with local periodicity [11]. Rank-N describes a composite material composed of N differently oriented layers. For a single loading condition, the optimal laminate can be described by two orthogonally oriented layers, i.e., rank-2 laminate, simplified as a square cell with a rectangular hole in homogenization-based topology optimization [11]. Orienting the rank-2 laminate according to the principal stress directions resulting from the single loading would create a stiff structure. However, under multiple loading conditions, there are principal stress directions associated with each of the loading conditions. Intuitively, multiple rank-2 laminates shall be superimposed, each accounting for the principal stress directions from one of the loading conditions. Instead of superimposing multiple rank-2 laminates, one needs to resort to laminates with a higher rank. It has been shown that rank-3 laminates are a good option for multiple loading conditions in 2D. They provide the needed design freedom to account for multiple loading conditions, while avoiding the increased computational complexity and numerical instability during optimization when laminates with an even higher rank are used [22]. Fig. 2 visually compares the structures optimized for single loading conditions using rank-2 laminates (b and d), and the structure optimized for multiple loading conditions using rank-3 laminates (e).

The rank-3 laminate is constructed by piling up three layers of materials that orient differently, yet assuming perfect bound condition among different layers [22,24,25]. On each layer, two phases of material are considered, i.e., stiff material (+) and

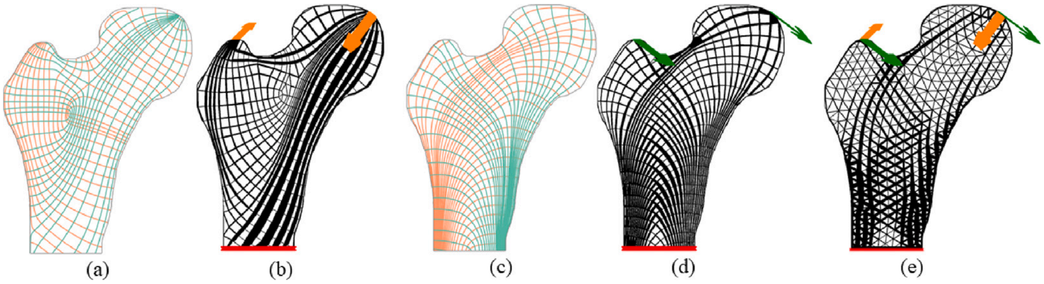

Fig. 2. (a) and (c): the principal stress lines in the object under two different loading conditions, F_1 (orange) and F_2 (green). (b) and (d): the correspondingly optimized structures based on rank-2 laminates, obtained using a de-homogenization approach for a single loading condition [13]. (e) Optimized structures for both loading conditions, obtained using our proposed approach based on rank-3 laminates. (For interpretation of the references to colour in this figure legend, the reader is referred to the web version of this article.)

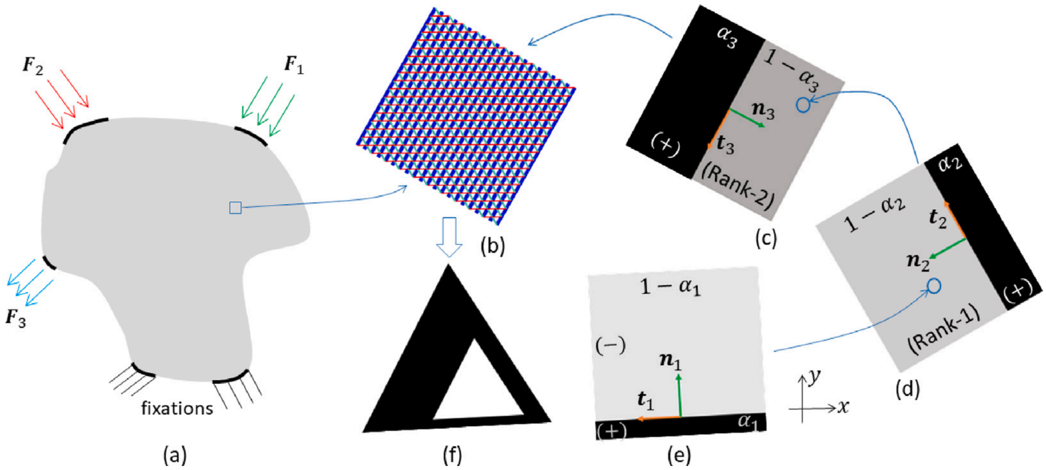

Fig. 3. Illustration of the composition of a rank-3 laminate and its geometric interpretation. (a) The design domain and boundary conditions, where each simulation cell is depicted by a set of specifications of a rank-3 laminate. (b) The multi-scale rank-3 laminate in a selected simulation cell. The material is composed of three differently oriented layers, shown in (c), (d), and (e), respectively. α is the relative width of each layer. $\boldsymbol{n}$ and $\boldsymbol{t}$ refer to the normal and tangent direction of a layer, respectively. (f) The proposed single-scale geometric interpretation of the rank-3 laminate as an equilateral triangle, with a unique thickness per edge.

compliant material (−). The stiff material indicates an isotropic solid material deposition, while the compliant material varies among the different layers.

Fig. 3 illustrates the composition of a rank-3 laminate, assuming given boundary conditions Fig. 3a and a unit-size macro-cell with multi-scale rank-3 laminate Fig. 3b. The base layer is layer 3, i.e., the rank-3 laminate is constructed by starting from layer 3 (Fig. 3c). The solid material deposition (ρ_3) on layer 3 is then described by the width variable α_3 and the compliant material $1-\alpha_3$. The compliant material is rank-2. Sequentially on layer 2 with width variable α_2 for the solid material (Fig. 3d), the remaining region to fill is $1-\alpha_3$. The actual consumption of solid material (ρ_2) on layer 2 is $(1-\alpha_3)\alpha_2$. Correspondingly, the compliant material on layer 2 is rank-1, and its volume fraction is $(1-\alpha_3)(1-\alpha_2)$. On layer 1 with width variable α_1 (Fig. 3e), the solid material consumption (ρ_1) is $(1-\alpha_3)(1-\alpha_2)\alpha_1$, and the corresponding compliant material is 'void', with a ratio of $(1-\alpha_3)(1-\alpha_2)(1-\alpha_1)$. The 'void' material is assigned a small Young's modulus E^- to avoid numerical instabilities, yet which is negligible compared to the Young's modulus E^+ of the solid material (i.e., $E^- = 10^{-6}E^+$). The Poisson's ratio υ_0 of void material is the same as that of the solid material. The orientation of layer n is described by its normal $\boldsymbol{n}_n$ and tangent $\boldsymbol{t}_n$, as depicted in Fig. 3. Through this process, the volume fraction of a rank-3 cell with unit size can be described by

$$\rho = 1 - \prod_{n=1}^{3}(1-\alpha_n). \tag{1}$$

Alternatively, the volume fraction can be described by

$$\rho = \rho_1 + \rho_2 + \rho_3. \tag{2}$$

Here, $\rho_1 = (1-\alpha_3)(1-\alpha_2)\alpha_1$, $\rho_2 = (1-\alpha_3)\alpha_2$, and $\rho_3 = \alpha_3$.

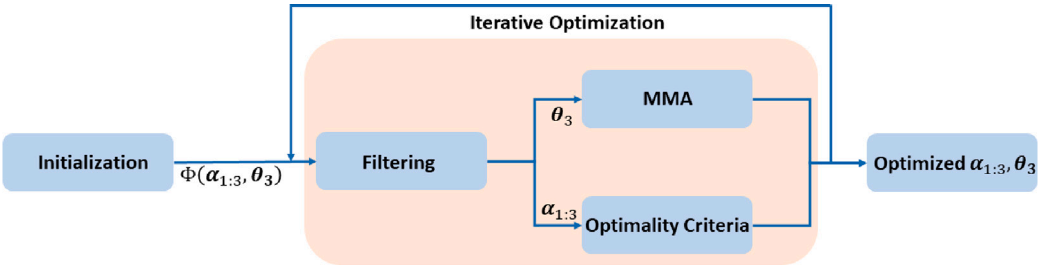

Fig. 4. Flowchart of homogenization-based topology optimization using a triangular interpretation of rank-3 laminates.

An interpretation of a rank-3 laminate as a triangular structure is illustrated in Fig. 3f. A general rank-3 laminate can be described by six parameters, i.e., three width variables $(\alpha_1, \alpha_2, \alpha_3)$ and three orientation variables $(\theta_1, \theta_2, \theta_3)$. However, allowing the orientation variables to change independently of each other may result in triangles with bad aspect ratio (i.e., sliver triangles). To improve the geometric regularity of the de-homogenized triangular lattice, we propose to reduce the design space by allowing only equilateral triangles, i.e., by letting $\theta_2 = \theta_3 + \frac{\pi}{3}$ and $\theta_1 = \theta_3 + \frac{2\pi}{3}$. Consequently, the independent design variables become $\alpha_1, \alpha_2, \alpha_3$ and θ_3. The restriction of possible edge orientations has a consequence on the mechanical performance of the optimized structures. Our experiments demonstrate a rather weak stiffness decrease, i.e., less than 5% in various tests, yet the geometric regularity is significantly improved. Furthermore, this restriction positively affects the numerical convergence of the optimization process, as it reduces the discontinuities in the optimized laminate configurations.

2.2. Homogenization-based topology optimization

In topology optimization, the objective function quantifies the design target with respect to the corresponding design variables. The optimization process minimizes the objective function by iteratively adjusting the design variables. For designing stiff structures, the objective function usually considers the strain energy, also known as compliance. For multiple loading conditions, the contributions from different loads need to be taken into consideration concurrently. Thus, a weighted summation of the strain energy subject to each loading condition is used as a compliance metric (C):

$$C = \sum_{q=1}^{M} w_q \boldsymbol{F}_q^T \boldsymbol{U}_q. \tag{3}$$

Here, M is the number of loading conditions, $\boldsymbol{F}_q$ is the nodal force vector of the $q-$th loading condition and $\boldsymbol{U}_q$ is the corresponding displacement vector obtained by solving the static equilibrium equation using finite element analysis. w_q is the weighting factor of the $q-$th loading condition, with $w_q = \frac{1}{M}$, $q = 1 : M$ in our implementation.

Let O be the objective function considering the compliance metric C. By taking triangular lattices as design parameters, homogenization-based topology optimization can be formulated as

$$\min_{\boldsymbol{\alpha}_1,\boldsymbol{\alpha}_2,\boldsymbol{\alpha}_3,\boldsymbol{\theta}_3} \quad O(\boldsymbol{\alpha}_1, \boldsymbol{\alpha}_2, \boldsymbol{\alpha}_3, \boldsymbol{\theta}_3), \tag{4}$$

$$\text{subject to} \quad \boldsymbol{K}(\boldsymbol{\alpha}_1, \boldsymbol{\alpha}_2, \boldsymbol{\alpha}_3, \boldsymbol{\theta}_3)\boldsymbol{U}_q = \boldsymbol{F}_q, \quad q = 1 : M, \tag{5}$$

$$\frac{1}{N_e} \sum_e \rho_e - V_F \leq 0, \tag{6}$$

$$L_{min} \leqslant \boldsymbol{\alpha}_1, \boldsymbol{\alpha}_2, \boldsymbol{\alpha}_3 \leqslant L_{max}, \tag{7}$$

$$-4\pi \leqslant \theta_3 \leqslant 4\pi. \tag{8}$$

Here, $\boldsymbol{K}$ is the global stiffness matrix assembled from the element stiffness matrices $\boldsymbol{K}_e$. $\boldsymbol{K}_e = \int_{\Omega_e} \boldsymbol{B}^T \boldsymbol{S} \boldsymbol{B}\, \mathrm{d}x$, with $\boldsymbol{B}$ being the element strain matrix and $\boldsymbol{S}$ the elasticity tensor of the rank-3 laminate. The elasticity tensor of the rank-n laminate can be determined analytically [24–26]. In Appendix, we derive $\boldsymbol{S}$ for the rank-3 laminate. N_e is the number of simulation cells, $\boldsymbol{\rho}_e$ corresponds to the relative density value of each cell (Eq. (1)). V_F is the threshold of the volume fraction to control the material budget. L_{min} and L_{max} describe the lower and upper bounds of the layer widths during optimization, respectively, with $0 < L_{min} < L_{max} < 1$. The lower bound L_{min} is introduced to avoid the appearance of large regions that are fully empty in the design domain, and the upper bound L_{max} is used to avoid fully solid regions. We set the range of $\boldsymbol{\theta}_3$ according to Krog et al. [24].

We utilize a hybrid scheme for solving the optimization problem (see Fig. 4 for an overview of the optimization process). The three width variables $\alpha_1, \alpha_2, \alpha_3$ are updated by a standard optimality criteria [27], and the orientation variable θ_3 is updated by the *Method of Moving Asymptotes* (MMA) [28]. We found that a moving step size of 0.01 for the layer widths and $\frac{\pi}{180}$ for their orientations resulted in a good balance between convergence speed and quality. A standard convolution filter [29,30] is applied to the width and orientation variables for improved numerical robustness.

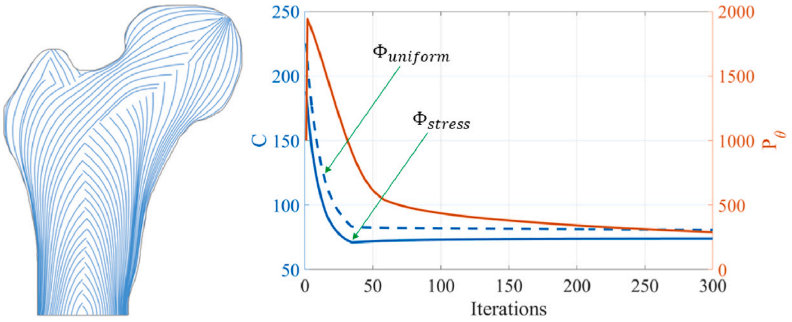

(a)

(b)

Fig. 5. (a) Streamlines in the initial orientation field. (b) Compliance and orientation regularization over the scope of the optimization process.

2.2.1. *Orientation regularization*

As mentioned in Section 2.1, when using an anisotropic rank-3 laminate the optimal solution is not unique. I.e., while the design variables of each cell can locally converge to the optimum, they might not form a continuous design specification globally. Since this prevents the generation of a consistent structure in de-homogenization, regularization is needed to counteract or at least mitigate this non-uniqueness issue.

We adapt a regularization method for orientations [22] to alleviate the potential discontinuity of the optimized orientation $\boldsymbol{\theta}_3$. Specifically, we include a per-edge penalty term in the objective function, i.e., for two adjacent elements e_i and e_j with shared edge e_{ij}

$$P^{\theta}_{e_{ij}} = \frac{1}{2} - \frac{1}{2}\cos\left(h_0 \cdot (\theta_3(e_i) - \theta_3(e_j))\right). \tag{9}$$

For each cell e_i, its adjacent cells are defined as the cells sharing an element edge with e_i. $P^{\theta}_{e_{ij}}$ with values between 0 and 1 quantifies the orientation deviation between two adjacent cells. Considering only the orientation variable, a rotation of an equilateral triangle by $\frac{\pi}{3}$ is invariant. Thus we set $h_0 = 6$. The orientation deviation between adjacent cells becomes zero if $\theta_3(e_i) - \theta_3(e_j) = k\frac{\pi}{3}$ (k is an integer). Accordingly, the largest deviation occurs when $\theta_3(e_i) - \theta_3(e_j) = k\frac{\pi}{3} + \frac{\pi}{6}$, leading to $P^{\theta}_{e_{ij}} = 1$.

Let N^i_e be the number of cells adjacent to the considered cell e_i, and $P^{\theta}_{e_{ij}}$ the orientation deviation of a cell e_i to its $j-$th adjacent cell. Then, a global measure of the orientation deviation across the design domain is given by

$$P^{(\theta)} = \sum_{i=1}^{N_e}\sum_{j=1}^{N^i_e} P^{\theta}_{e_{ij}}. \tag{10}$$

Now the objective function becomes a weighted summation of the compliance and the orientation regularization

$$O(\boldsymbol{\alpha}_1, \boldsymbol{\alpha}_2, \boldsymbol{\alpha}_3, \boldsymbol{\theta}_3) = W\frac{C}{C^*} + (1 - W)\frac{P}{P^*}. \tag{11}$$

The weighting factor W takes on values in $(0,\ 1]$. C^* and P^*, respectively, refer to the compliance and the orientation regularization corresponding to the initial values of the design variables. Orientation regularization can be disabled by setting $W = 1$. In all of our experiments, we have set $W = 0.5$.

2.2.2. *Initialization*

The outcome of the non-convex optimization depends on the initial values of the width and orientation variables. Different initializations may lead to different density layouts and also affect the convergence behavior of the optimization process. In previous works, these dependencies have been demonstrated for single [31,32] and multiple [22] loading conditions. The initialization is particularly important since the optimal solution of a rank-3 laminate is not unique, i.e., different values of the width and orientation variables may lead to the same elasticity tensor [33].

We take inspiration from the work by Jensen et al. [22], where the initial principal stress directions are used to construct the initialization. We adapt it for our triangular infill model. This adaptation considers that only the orientation of layer 3 is considered independently in our framework, i.e., only a single direction field is involved. Specifically, we first compute the principal stress fields of the fully solid domain subject to the M loading conditions respectively, resulting in $2 \times M$ principal stress values and the corresponding principal stress directions for each simulation cell. For each simulation cell, we choose the principal stress direction $\boldsymbol{\theta}_p$ with largest magnitude as the initial orientation of layer 3.

It is worth noting that the orientation variable in rank-3 is represented by the normals of each layer, while the 'dominant' principal stress direction is supposed to indicate the layering orientation, i.e., the layer tangent. Thus, $\boldsymbol{\theta}_p + \frac{\pi}{2}$ is used as the initial value of $\boldsymbol{\theta}_3$ in the optimization. For the initialization of the width variable, we simply let $\boldsymbol{\alpha}_n = \frac{V_F}{3}$, $n = 1 : 3$. Fig. 5a shows the principal stress-based initialization $\boldsymbol{\Phi}_{stress}$ via streamlines in the direction field $\boldsymbol{\theta}_p + \frac{\pi}{2}$. The variation of the compliance C and orientation regularization P_θ are shown in Fig. 5b. The optimized design is shown in Fig. 1. For comparison, Fig. 5b also shows the

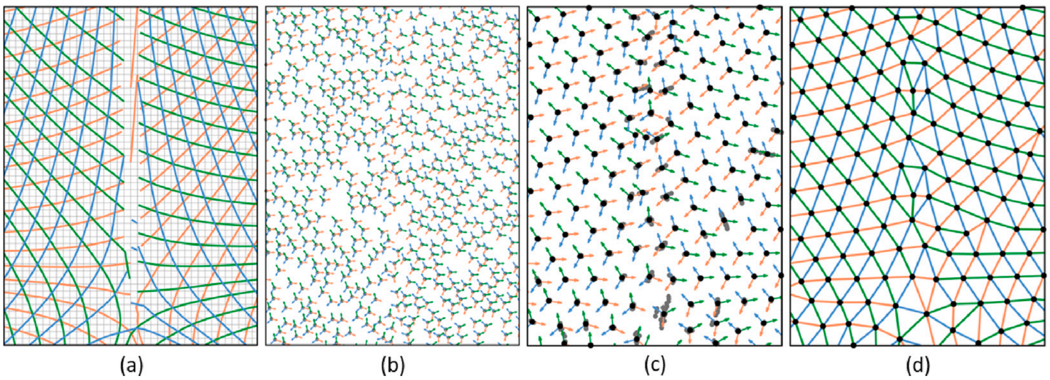

Fig. 6. (a) The domain discretization (background) and streamlines in the three different orientation fields of an optimized 6-RoSy field. (b) The randomly distributed positions (and respective directions) used for position optimization. The distribution is generated by considering a pre-defined edge length of the output mesh and the resolution of the input grid. (c) The position field after optimization and the representative positions (black dots) used to construct the output mesh. (d) The output mesh whose edges align with the optimized orientation field. Orientations are indicated by arrows, and edge colors distinguish corresponding layer orientations. To reduce visual clutter, only three of the six pairwise bidirectional 6-RoSy field directions are illustrated. (For interpretation of the references to colour in this figure legend, the reader is referred to the web version of this article.)

optimization history of the compliance when a uniform initialization $\Phi_{uniform}$ is used, where $\theta_3 = \frac{\pi}{2}$. Here, to release more design space, orientation regularization is omitted. It is seen that the optimization process converges to a smaller compliance value when using Φ_{stress} instead of $\Phi_{uniform}$.

Fig. 5a shows that the proposed initialization does not necessarily yield a globally continuous direction field. This, however, does not pose a problem for our approach. On the one hand, due to the use of orientation regularization, the direction field is smoothed to the maximum extent during optimization. On the other hand, the proposed geometry-based de-homogenization is less sensitive to the potential local discontinuity.

3. De-homogenization using field-aligned triangulation

Our proposed de-homogenization process converts the optimized spatially varying specifications $(\alpha_1, \alpha_2, \alpha_3, \theta_3)$ into a structural design. The conversion includes three steps. Firstly, we create an equilateral triangle mesh with its edges following the layer orientations. Secondly, we assign a thickness to each edge – determined from the optimized layer widths $(\alpha_1, \alpha_2, \alpha_3)$ – to create a spatially graded triangular lattice structure. Lastly, we create a globally consistent lattice structure by adjusting the edge thicknesses at the vertices where multiple edges meet.

3.1. Field-aligned triangulation

In the first step, we use field-aligned triangulation [23] to generate an equilateral triangle mesh whose edges are aligned with the rank-3 layer orientations. In the following, we give a brief overview of the used triangulation and its adaptation to our application scenario. The triangulation is performed in three subsequent steps:

- ***Orientation field optimization***. We compute an orientation field comprising a set of directions to which the edges of the output mesh should be aligned. The smoothness of this field is achieved by a Gauss–Seidel process.
- ***Position field optimization***. A local parametrization (vertex positions) is computed so that the edges between vertices are aligned with the optimized orientation field.
- ***Mesh extraction***. The computed orientation and position fields are turned into a graph structure from which a triangular mesh is constructed.

In the original field-aligned triangulation [23], the direction field is a smooth 6-RoSy field.[1] This field aligns with the features on the boundary domain and is obtained by optimizing from a set of randomly distributed orientations. In the context of de-homogenization, the direction field represents the optimized layer orientations. Thus, the original method is adjusted to take the optimized layer orientations as input, and then perform position field optimization and mesh extraction sequentially. This is illustrated in Fig. 6. Given a discretization of the domain by a grid, guided by our generated orientation field that is visualized by streamlines, we apply the triangulation method to convert the orientation field into a triangle mesh with its edges following the orientation field.

---

[1] The 6-RoSy field refers to a 6-rotational symmetric field, which intuitively represents phenomena that are invariant under rotations of an integer multiple $\frac{2\pi}{6}$ [34,35].

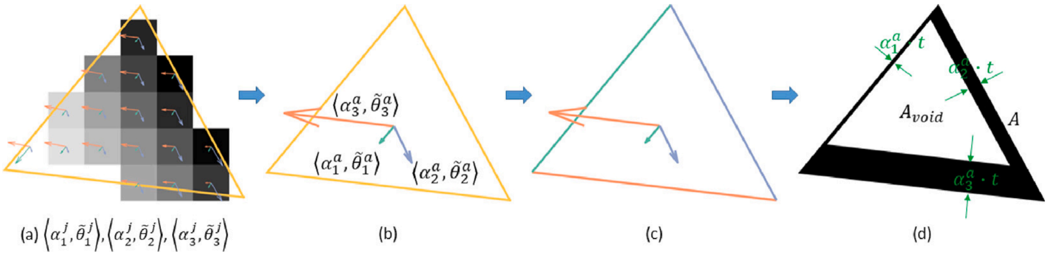

Fig. 7. Lattice element de-homogenization. (a) A field-aligned triangular element with its covered cells. $\tilde{\theta}_i^j$ refer to the tangents of layers $i \in 1,2,3$ in element j. For each cell, three arrow glyphs indicate the tangents. Corresponding width variables α_i^j are encoded into the arrow lengths. (b) Widths and orientations at a single cell. (c) Relation between representative layer orientations and corresponding edges of the triangular element, determined via their orientation deviations. (d) The de-homogenized triangular lattice element whose unique edge thicknesses reflect the representative values of widths. The solid regions correspond to the deposition ratio indicated in (a).

3.2. Anisotropic triangle mesh

De-homogenization is performed on a per-triangle basis. As shown in Fig. 7a, each triangular element covers a certain region in the domain. The target deposition ratio v_k^* of the kth triangular element is measured by $\frac{\rho_k}{M_k}$, where M_k is the number of cells located in the region covered by the triangular element, and ρ_k is the sum of the density values over all these cells. The available material in each triangular region should be re-distributed so that (i) a binary material layout is generated, (ii) a continuous transition at the element boundaries is obtained, and (iii) the specific depositions (layer widths optimized with respect to the object's compliance) on each oriented layer of the cells is reflected in the binary material layout. I.e., the underlying anisotropy of the optimized cells should be preserved in the de-homogenized lattice elements. In cases where the triangular mesh has a similar or higher resolution than the rank-3 simulation cells, the specifications of the cells are resampled using bilinear interpolation so that each triangular element covers at least a certain number of cells, (e.g., ≥ 10).

De-homogenization requires that the de-homogenized triangular elements maintain their deposition ratios, i.e.,

$$\frac{\rho_k}{M_k} = \frac{A - A_{void}(t)}{A} \tag{12}$$

Here, A is the area of the triangular element, and A_{void} is the area of the void region left in the triangular element after de-homogenization (Fig. 7d). t is the thickness parameter that needs to be determined to satisfy the equation. The void area A_{void} is up to the edge thicknesses of the triangular element. To convey the anisotropy via the edge thickness, for each edge, respectively, t is scaled by the scaling factors α_1^a, α_2^a and α_3^a (Fig. 7b), which are determined by the representative values of the actual material deposition on each layer.

For each cell j covered by a triangular element, the material depositions of each layer are evaluated according to Eq. (2), i.e.,

$$\begin{aligned}
\hat{\alpha}_1^j &= (1-\alpha_3^j)(1-\alpha_2^j)\alpha_1^j \\
\hat{\alpha}_2^j &= (1-\alpha_3^j)\alpha_2^j \\
\hat{\alpha}_3^j &= \alpha_3^j.
\end{aligned} \tag{13}$$

α_1^j, α_2^j, and α_3^j are the corresponding width variables of layer 1, 2, and 3 of the jth cell, respectively. From Eq. (13), the representative values (α_1^a, α_2^a and α_3^a) of the actual material deposition along each layering orientation in a triangular element are given by $\alpha_1^a = \sum_{j=1}^{M_k}\hat{\alpha}_1^j$, $\alpha_2^a = \sum_{j=1}^{M_k}\hat{\alpha}_2^j$, and $\alpha_3^a = \sum_{j=1}^{M_k}\hat{\alpha}_3^j$, respectively. In practice, α_1^a, α_2^a and α_3^a are normalized by $\max(\alpha_1^a,\alpha_2^a,\alpha_3^a)$.

Relating each edge of the triangular element to the corresponding layer orientation is required to convey the anisotropy of the underlying cells. However, since the orientations vary across the cells, in general, representative orientations first need to be computed. Here, we make use of a weighted average strategy, i.e., the actual material deposition on each layer is used to weight the corresponding orientation. With $\tilde{\theta}_i^j$ referring to the tangent of layer i of the jth cell within the triangular element, the weighted average is computed as

$$\tilde{\theta}_i^a = \frac{\sum\limits_{j=1}^{M_k}\tilde{\theta}_i^j\hat{\alpha}_i^j}{\sum\limits_{j=1}^{M_k}\hat{\alpha}_i^j}, \quad i = 1:3. \tag{14}$$

We let the mesh edges correspond to $\tilde{\theta}_1^a$, $\tilde{\theta}_2^a$ or $\tilde{\theta}_3^a$, depending on which edge they have the least directional deviation (see Fig. 7c).

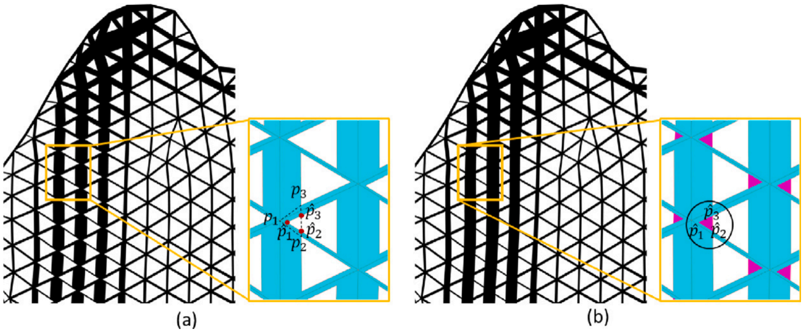

Fig. 8. (a) The structural design after de-homogenization. (b) Gaps are filled with additional triangles.

3.3. Lattice structure

When considering triangular elements, per-lattice de-homogenization does not necessarily produce a well-posed structural design. This is because gaps are introduced at shared mesh vertices where edges with different thicknesses meet, see Fig. 8a. To avoid this issue, we use additional triangular elements to fill these gaps.

In particular, we first determine those triangular lattice elements that need to be fixed. At the vertex p_1 where the gap occurs, a filling triangle is inserted. Firstly, for each of the two edges leaving p_1, the two vertices of the empty triangles on either side of this edge are considered, i.e., p_2 and p_3 in Fig. 8b. Then, it is checked whether the corresponding vertex of the internal empty triangle of the considered lattice $\hat{p}_1$ is within the triangle $S_{p_1 p_2 p_3}$. If $\hat{p}_1$ is outside of $S_{p_1 p_2 p_3}$, no gap needs to be filled. Otherwise, a solid triangle $S_{\hat{p}_1 \hat{p}_2 \hat{p}_3}$ is placed, where $\hat{p}_2$ and $\hat{p}_2$ are the intersection points of $p_2 p_3$ and the corresponding edges of the empty triangle in the considered lattice. In this way it is ensured that there is no material overlap in the final structural design (see Fig. 8b). The additional material consumption of the gap-filling triangles is compensated by down-scaling the deposition ratio in Eq. (12) accordingly.

4. Results

In the following, we perform a number of experiments to assess the quality of our proposed method. Firstly, we perform a parameter study to analyze the behavior of our method with respect to different settings. This includes the different initialization strategies with and without orientation regularization, and the different resolutions of the triangular parametrization. Secondly, we compare our results to those of alternative approaches, including the uniform triangular lattice structure, the porous infill structure produced by density-based topology optimization under a local volume constraint [3], and the alternative de-homogenization approach [22]. We then consider two practical use cases to further verify the practicability of our method. Finally, the adaptivity to situations with concurrently varying loading and constraint conditions is demonstrated via a specific test case. To differentiate our approach from alternative approaches, our generated structural design is presented by a density layout in black together with the corresponding triangular mesh in green. This highlights both the structural design and an explicit geometric format produced by our approach.

In all examples, the design domains are discretized by Cartesian grids with unit size. Young's modulus and Poisson's ratio are set to 1.0 and 0.3, respectively. Except for field-aligned triangular meshing, which is performed with the open source software *Instant-meshes*[2] provided by Jakob et al. [23], all other approaches, including homogenization-based topology optimization and de-homogenization, are implemented in MatLab. We let the optimization process terminate after 300 iterations. The lower and upper bounds of the relative width of each cell are set to $L_{min} = 0.1$ and $L_{max} = 0.5$, if not said otherwise. Correspondingly, the relative density value varies from 0.271 to 0.875 according to Eq. (1). All experiments have been carried out on a desktop PC with an Intel Xeon CPU at 3.60 GHz.

Performance statistics for all examples are given in Table 1. We also provide the resulting compliance C^* of homogenization-based topology optimization without restricting the layer orientations, i.e., all three orientation variables ($\theta_{1:3}$) can be adjusted arbitrarily during optimization. All other settings are kept the same as for generating C_0. By comparing C_0 to the corresponding C^*, we observe an increase in compliance due to the additional orientation constraint, i.e., within 5% (measured by $\frac{C_0 - C^*}{C^*}$) in all of the experiments using the proposed Φ_{stress} and orientation regularization.

Our method first performs homogenization-based topology optimization on a simulation mesh ($\mathfrak{R}_{sim}$) with low resolution to obtain the optimized specification. Then, the de-homogenized structural design is generated in the form of a triangular mesh with edges of load dependent thickness. To evaluate and compare the obtained designs, we also use a high-resolution validation mesh ($\mathfrak{R}_{fine}$). This is because the obtained structural design can be composed of very fine geometric details, which can only be captured

---

[2] https://github.com/wjakob/instant-meshes.

Table 1

Performance statistics for homogenization-based topology optimization and field-aligned triangulation-guided de-homogenization. C_0 and V_0, respectively, are the compliance and volume fraction of the optimal layout resulting from homogenization-based topology optimization. Accordingly, C and V correspond to the de-homogenized result. The design deviation of the de-homogenized result from the optimal layout is evaluated by $\xi = \frac{C\cdot V - C_0\cdot V_0}{C_0\cdot V_0}$. t_0 and t are the time consumptions of homogenization-based topology optimization and de-homogenization, respectively. Provided the same volume fraction, C^* is the resulting compliance of homogenization-based topology optimization without restricting the layer orientations.

Examples		Homogenization-based Opti.				De-homogenization			ξ
		C^*	C_0	V_0	t_0 (s)	C	V	t (s)	
Femur	Fig. 1d	73.34	76.86	0.50	366	84.37	0.50	25	9.78%
	Fig. 9c	75.26	83.25	0.50	356	92.17	0.50	27	10.93%
	Fig. 9f	71.25	73.30	0.50	354	84.19	0.50	30	14.86%
	Fig. 9i	73.34	76.86	0.50	366	85.01	0.50	29	10.60%
Wheel	Fig. 11b	7.78	8.03	0.50	280	8.30	0.50	27	3.29%
Beam	Fig. 12b	2.61	2.66	0.30	212	2.78	0.31	21	8.00%
Bracket 1	Fig. 13c	19.46	19.92	0.50	326	20.45	0.50	28	2.67%
Bracket 2	Fig. 13f	26.67	27.45	0.50	641	29.50	0.50	37	7.47%
Triangle	Fig. 14b	11.05	11.07	0.50	539	12.12	0.50	33	10.15%

Table 2

Statistics for the validation meshes ($\mathfrak{R}_{fine}$) used to evaluate the final structural designs, the simulation meshes ($\mathfrak{R}_{sim}$) used for homogenization-based topology optimization, and the triangular lattice elements (*#Lattice*) used for de-homogenization.

Examples		$\mathfrak{R}_{fine}$		$\mathfrak{R}_{sim}$		*#Lattice*
		#Resolution	*#Elements*	*#Resolution*	*#Elements*	
Femur	Fig. 1a	1200 × 1200	632,468	116 × 150	10,118	684 (Fig. 1f)
Wheel	Fig. 11a	1600 × 1600	1,930,188	100 × 100	7,740	1637 (Fig. 11b)
Beam	Fig. 12a	1600 × 800	1,280,000	100 × 50	5,000	699 (Fig. 12b)
Bracket 1	Fig. 13a	2296 × 1328	2,181,496	144 × 84	8,749	2101 (Fig. 13c)
Bracket 2	Fig. 13d	2332 × 1000	1,144,564	292 × 126	18,271	1167 (Fig. 13f)
Triangle	Fig. 14a	1360 × 1184	790,132	170 × 148	12,652	1065 (Fig. 14b)

by a sufficiently high resolution in compliance evaluation using finite element analysis. To enforce consistent boundary conditions independent of the resolution of the design, the design domain is first discretized into a fine Cartesian mesh as $\mathfrak{R}_{fine}$. From this mesh a coarse resolution grid ($\mathfrak{R}_{sim}$) and corresponding boundary conditions are constructed for homogenization-based topology optimization and subsequent de-homogenization. When evaluating the compliance of the obtained design, the triangular lattice structure is discretized according to $\mathfrak{R}_{fine}$, by identifying the cells of $\mathfrak{R}_{fine}$ that are located on the obtained triangular lattice edges. To ensure consistent boundary conditions and discretization when comparing C_0 and C, C_0 is re-evaluated after optimization by projecting the optimized specifications onto $\mathfrak{R}_{fine}$ through bilinear interpolation. For density-based topology optimization, $\mathfrak{R}_{fine}$ is directly used in the simulation to provide sufficient design space. Table 2 provides information regarding the resolution and number of elements of $\mathfrak{R}_{fine}$ and $\mathfrak{R}_{sim}$, as well as the number of triangular lattices involved in de-homogenization. The number of triangular lattices is determined as follows: First, a reference length for the triangular lattice edges is specified. This reference considers the preferred fineness of the structural design and a possible size limitation stemming from a downstream manufacturing task. Since the triangular lattices are from a set of approximately equilateral triangular elements, a reference area of the triangular lattices can then be derived from the reference length. Finally, the number of triangular lattices is computed by dividing the total area of the design domain by the reference area.

Design verification. With the 'Femur' model shown in Fig. 1 as an example, de-homogenization is performed using several test settings to verify our design decisions. Specifically, the results when using a uniform initialization $\boldsymbol{\Phi}_{uniform}$ and of original homogenization-based topology optimization, i.e., no orientation regularization is used, are given Fig. 9a–c. Fig. 9d–f shows the results the principal stress-guided initialization $\boldsymbol{\Phi}_{stress}$ is used without orientation regularization. In Fig. 9g–i, the settings in homogenization-based topology optimization remain the same as in Fig. 1, i.e., the initialization $\boldsymbol{\Phi}_{stress}$ and orientation regularization is used, but a higher resolution of the triangular parametrization is chosen. Fig. 9(c), (f), and (i) use the consistent resolution for creating the field-aligned triangular mesh.

The test results in Figs. 9 and 1, and the statistics in Table 1 demonstrate that the design deviation between homogenization-based topology optimization and de-homogenization results do not exceed 15%, and most are around at 10%, regardless of whether the optimized orientation field is continuous or not. This demonstrates that the proposed de-homogenization has relaxed requirements on the optimized specifications.

In terms of design quality measured by compliance and geometric regularity, however, different design decisions lead to different results. Compared to homogenization-based topology optimization using $\boldsymbol{\Phi}_{uniform}$ (Fig. 9a, b), $\boldsymbol{\Phi}_{stress}$ improves the convergence behavior (Fig. 9d, e). The compliance is reduced from 83.25 to 73.30 (Fig. 9b, e). However, $\boldsymbol{\Phi}_{stress}$ incurs more discontinuities in the optimized orientation field. Though the de-homogenized lattice structure corresponding to $\boldsymbol{\Phi}_{uniform}$ (Fig. 9c) is less stiff than the one obtained with $\boldsymbol{\Phi}_{stress}$ (Fig. 9f), the former design gives better geometric regularity. The difference in the setting for Fig. 9d, e and

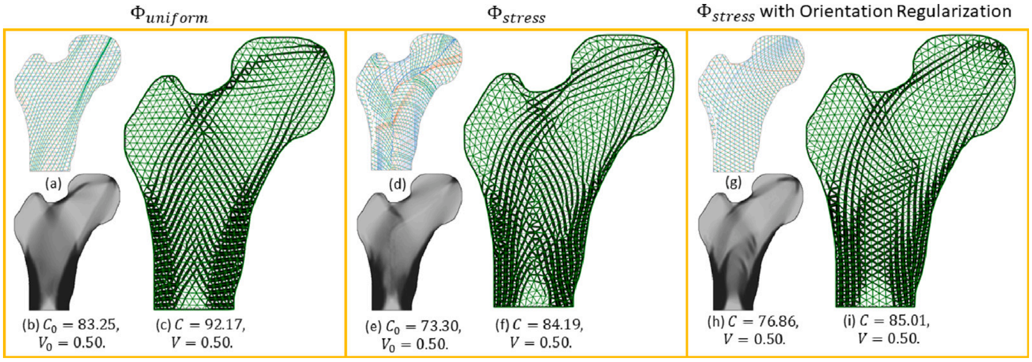

Fig. 9. The homogenization-based results (optimized orientations and density layout) and the corresponding de-homogenization results of three different settings are demonstrated in each box. In the left box (a–c), the homogenization-based topology optimization is conducted with the uniform initialization ($\Phi_{uniform}$). In the middle one (d–f), $\Phi_{uniform}$ is replaced with the proposed initialization Φ_{stress}, whereas other settings are kept the same. In the right box, both the Φ_{stress} and orientation regularization are considered in the homogenization-based topology optimization. Among (c), (f), and (i), the resolution of the used triangular meshes is consistent.

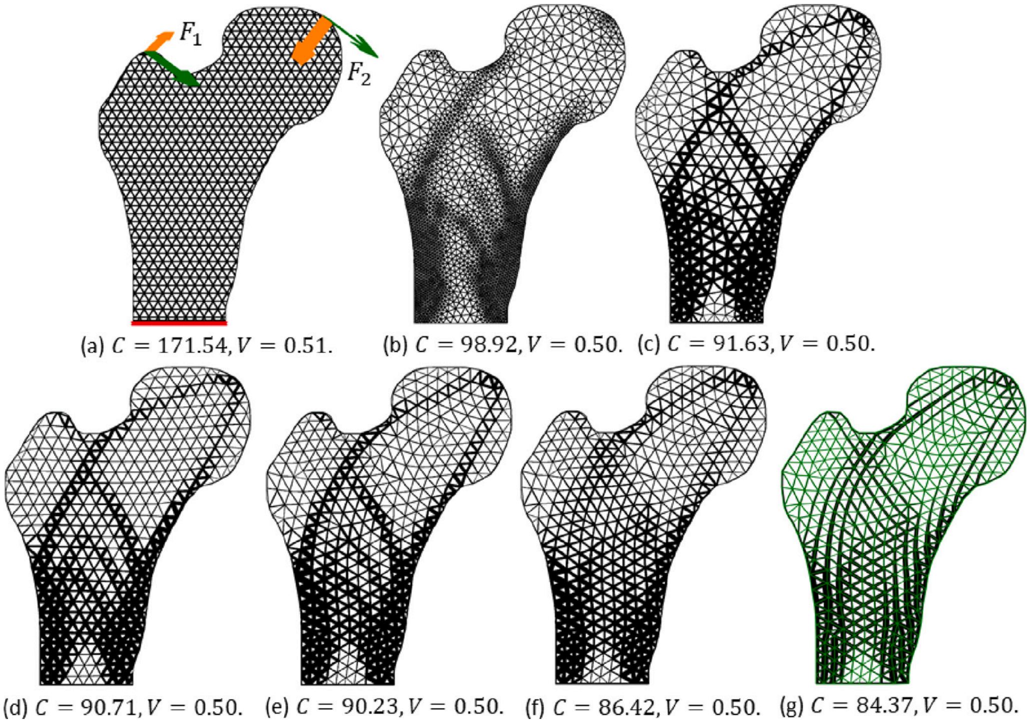

Fig. 10. Comparison of two optimization strategies and different triangulation-based interpretations. (a) A lattice structure consisting of regular triangles with uniform edge thickness across the domain. In (b–e), the optimized density field is interpreted using different triangulations. This density field is obtained using isotropic material properties in a SIMP-like topology optimization. (b) A triangular lattice with uniform edge thickness across the domain, but varying sparsity according to the density field. (c) A triangular lattice with an almost uniform edge length, but varying edge thickness according to the density field. (d) A regular triangular lattice with varying edge thickness according to the density field. In (e, f, g), the triangle mesh is interpreted using different density fields. The triangle mesh is obtained using field-aligned triangulation, from the frame field obtained using the proposed approach. (e) With varying edge thickness according to the density field from the SIMP-like topology optimization, as in (b, c, d). (f) With varying edge thickness according to the proposed approach, but constant edge thickness in each triangle cell. (g) The proposed approach.

g, h is that the latter considers orientation regularization. As a result, Fig. 9g behaves more continuously than (Fig. 9d), yet (Fig. 9e) is slightly stiffer than Fig. 9h. This is because orientation regularization acts like an additional constraint in the optimization process. The same phenomenon is kept in the de-homogenized results. Interestingly, the corresponding de-homogenization result Fig. 9f is only slightly stiffer than the result in Fig. 9i, regardless of the introduced geometric regularity. This behavior is interesting due to the severe discontinuity of the optimized orientation field (Fig. 9d) that still hurts the precision of de-homogenization, though it does not necessarily lead to failure in the de-homogenization process. From Figs. 9i and 1f, we further see that the proposed

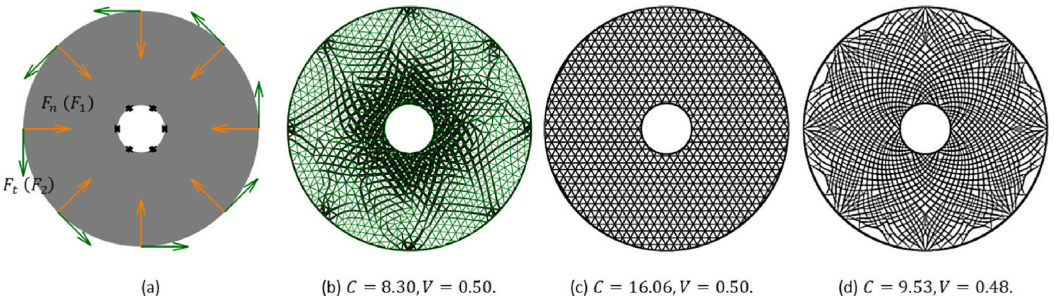

(a) (b) $C = 8.30, V = 0.50$. (c) $C = 16.06, V = 0.50$. (d) $C = 9.53, V = 0.48$.

Fig. 11. (a) A circular design domain with 2 different loading cases, the normal force F_n and shear force F_t. (b) Result by our method. (c) Uniform triangular lattice structure. (d) Porous infill structure.

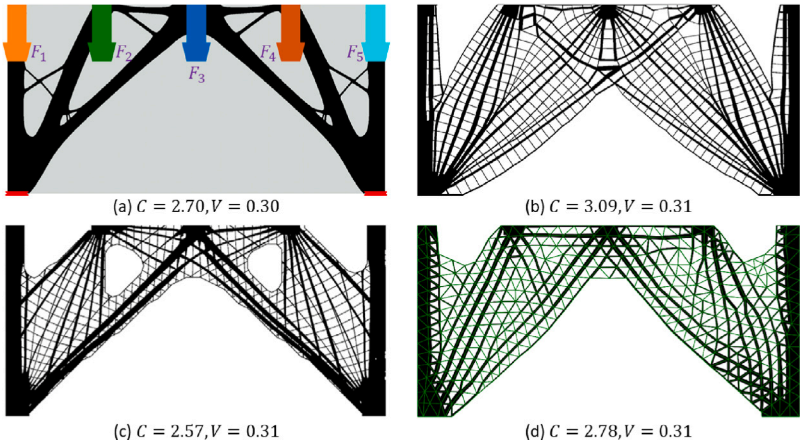

(a) $C = 2.70, V = 0.30$ (b) $C = 3.09, V = 0.31$

(c) $C = 2.57, V = 0.31$ (d) $C = 2.78, V = 0.31$

Fig. 12. (a) Rectangular design domain with 5 different loads (downward pointing arrows) and fixation areas at the bottom left and right (indicated by red dots). The inset shape is the design obtained with classic topology optimization. (b) The streamline-guided de-homogenization result using rank-2 as the micro-structure during optimization [13]. (c) The corresponding result with image-based de-homogenization [22]. (d) De-homogenized structural design by our method. (For interpretation of the references to colour in this figure legend, the reader is referred to the web version of this article.)

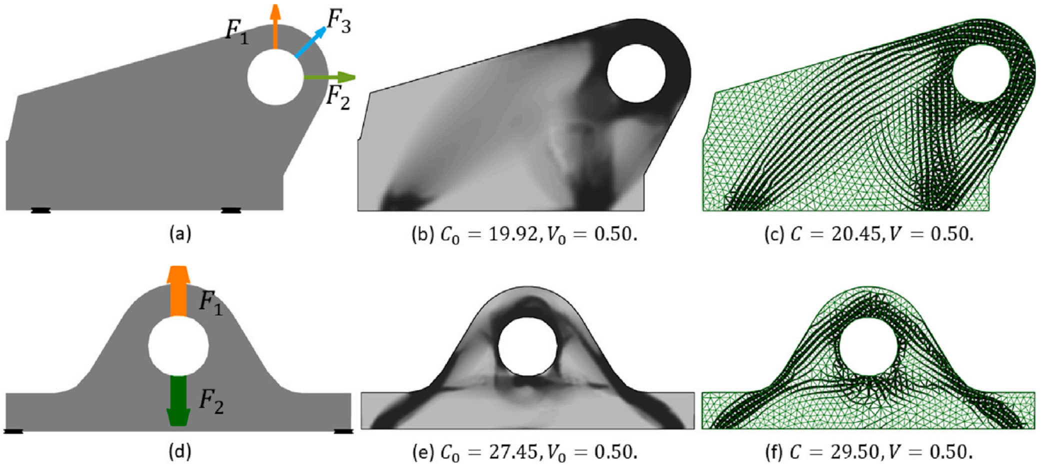

(a) (b) $C_0 = 19.92, V_0 = 0.50$. (c) $C = 20.45, V = 0.50$.

(d) (e) $C_0 = 27.45, V_0 = 0.50$. (f) $C = 29.50, V = 0.50$.

Fig. 13. (a), (d) Problem descriptions of bracket 1 and bracket 2, respectively. (b), (e) The corresponding density layouts generated by homogenization-based topology optimization. (c), (f) The resulting de-homogenized structural designs.

de-homogenization is stable with respect to changes of the triangular mesh resolution. By comparing Fig. 9c, f, and i, one can observe that the proposed homogenization-based topology optimization considering Φ_{stress} and orientation regularization achieves improved stiffness and geometric regularity concurrently. Thus, this setting is used in the following experiments.

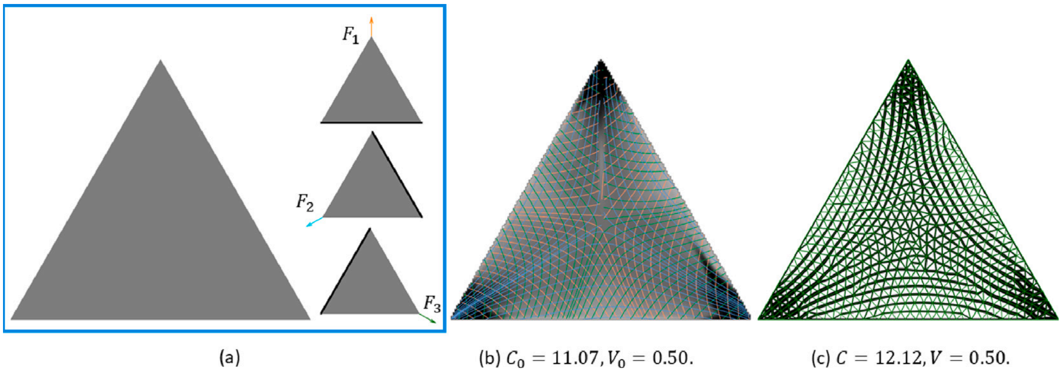

Fig. 14. (a) The equilateral triangular design domain and the corresponding boundary conditions. Here the thick lines in black indicate the fixation positions. The loads are shown in different colors, each load is outward of the design domain and perpendicular to the corresponding domain boundary. (b) The optimized density layout and the corresponding layer orientations shown by streamlines. (c) The de-homogenized triangular lattice structure. (For interpretation of the references to colour in this figure legend, the reader is referred to the web version of this article.)

Comparative analysis. We compare different triangulation-based interpretations and two optimization strategies. We modify our method to perform SIMP-like topology optimization, by fixing the orientation field (θ) and taking the layer width as an optimization variable. Furthermore, isotropic triangles are simulated by keeping the three width variables per cell the same, i.e., $\alpha_1 = \alpha_2 = \alpha_3$. The second optimization strategy is our proposed approach, which optimizes the triangle orientations and layer widths.

Fig. 10(a) shows a regular triangular lattice with uniform edge thickness across the domain. In (b), a density field is derived from the optimized per-triangle width and used to inform a Delaunay-based isotropic triangulation. The triangle elements are smaller where the density is higher. In (c) and (d), the optimized per-triangle width is mapped to a Delaunay-based isotropic triangulation and a regular triangular grid, respectively. Graded triangular lattices similar to (b, c, d) have been reported, for example, by Liu et al. [36]. In (e, f, g), the triangle mesh is obtained using field-aligned triangulation, using our proposed approach, yet the triangles are thickened differently. In (e), by the per-triangle constant width from the first optimization strategy, in (f) by the averaged per-triangle width from the proposed optimization strategy, and in (g), by the per edge thickness obtained by the proposed optimization strategy. The triangular lattices all have the same volume fraction of 0.50, except for (a) which is 0.51. The proposed optimization creates anisotropic triangular lattices with a compliance of 84.37, which is 6.49% smaller than the smallest from the SIMP-based optimization (b, c, d, e).

Fig. 11 shows another comparison, using a circular design domain with two loading conditions (a). The de-homogenized triangular lattice (b) is compared to a regular triangular lattice (c) and a porous infill using local volume constraints (d). The regular triangular lattice structure gives rise to the highest compliance. The de-homogenized triangular lattice structure from our method is slightly stiffer than the porous infill structure using density-based topology optimization. However, the latter requires a sufficiently high simulation resolution to obtain a fine structural design. This significantly increases the computational cost.

While our method is primarily developed to generate infill structures that spread across the entire design domain, it can be adapted to generate lattice structures that cover only parts of the design domain, by setting $L_{min} = 1.0 \times 10^{-6}$, $L_{max} = 1.0$. The obtained structural layout is a subset of the initial design domain. With this adaptation, we further compare our method to classic topology optimization and the existing de-homogenization approaches, confirming validity and evaluating the trade-off between the structural performance and regularity of the lattice.

The design domain and load conditions are illustrated in Fig. 12a, where the classic topology optimization result using SIMP is superimposed on the domain. In Fig. 12b, we conduct the rank-2-based homogenization-based topology optimization and utilize the streamline-guided de-homogenization to generate the structural design [13]. To counteract the non-uniqueness issue of principal stress directions in determining the optimal layer orientations of rank-2, we directly optimize the layer orientation via a gradient-based optimizer. The results from the image-based approach [22] and our method are shown in Fig. 12c and d, respectively. The structure generated by our method consists of equilateral triangles with varying thicknesses, while the image-based approach generates a large number of intersections of differently oriented beam-like substructures. Improved regularity of the lattice structures is achieved by compromising stiffness. The difference in stiffness is 8.2%, measured by $\frac{C_{ours} - C_{alternative}}{C_{alternative}}$, for the same volume fraction, with $C_{ours} = 2.78$ and $C_{alternative} = 2.57$. Besides this, our result exhibit stiffnesses en par with the classic topology optimization result and is stiffer than the rank-2-based de-homogenization results.

Mechanical parts. With 'Bracket-1' and 'Bracket-2' we consider two mechanical parts for emphasizing the basic features of the proposed de-homogenization scheme (see Fig. 13). In particular, the results are in line with those obtained for 'femur' concerning compliance and geometric regularity.

Multiple boundary conditions. We further demonstrate the adaptivity of the proposed method to the optimization problems with totally different boundary conditions, i.e., the fixations and loads vary concurrently. Here we consider an equilateral triangular design domain for infill optimization (Fig. 14a).

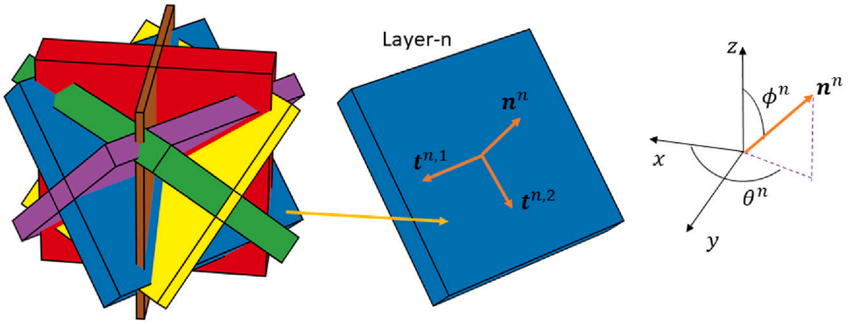

Fig. 15. Sketch of a single-scale approximation of a rank-6 laminate in 3D. $\boldsymbol{n}^n$ is the normal vector of layer-n, $\boldsymbol{t}^{n,1}$ and $\boldsymbol{t}^{n,2}$ are two corresponding tangent vectors.

In Fig. 14, we show the optimization and de-homogenization results, where the design deviation between the de-homogenized result and the corresponding homogenization-based topology optimization result is at $\xi = 10.15\%$ and close to other examples. In addition, the triangular lattice structure exhibits good regularity.

5. Conclusion and future work

In this paper, we have introduced an innovative geometry-based de-homogenization technique for designing and optimizing functionally graded triangular lattices capable of withstanding various loading conditions. By conducting simulations and optimizations at a low-resolution discretization of the design domain, our de-homogenization approach, akin to other methods in this domain, generates highly detailed structures with significantly reduced computational demands compared to traditional density-based topology optimization methods.

Unique to our approach is its ability to explicitly represent the resulting structural design in a concise geometric format, i.e., a global triangular mesh where each edge is assigned a distinct thickness. This explicit geometric representation facilitates downstream processes such as editing and additive manufacturing. In terms of mechanical performance, the de-homogenized structure exhibits stiffness comparable to that of the optimal design achieved through homogenization-based topology optimization. Additionally, when compared to porous infill generated using local volume constraints, our de-homogenized structure consistently demonstrates higher stiffness.

In the future, we aim to extend geometry-based de-homogenization towards 3D problems, i.e., to generate a stiffness-optimal structural design of sound geometric regularity and described in a compact geometric format. According to Ref. [25,37], in 3D a rank-6 laminate is needed to approach the theoretically optimal stiffness subject to multiple loading conditions. Just as we simplified a general rank-3 laminate to an equilateral triangle, we speculate that a general rank-6 laminate in 3D could potentially be approximated by an equilateral tetrahedron. We plan to verify this hypothesis and devise geometric techniques for the de-homogenization process. Fig. 15 shows a single-scale approximation of a rank-6 laminate. Here, we need three design variables to fully describe a single layer of a rank-6 laminate: one variable for the layer thickness and two independent variables for the layer orientation (normal vector). In total this amounts to 18 design variables. Although it is possible to reduce the number of independent design variables to 15 via a transformation process [38], finding a compatible field-aligned geometric parametrization is still challenging. To ease the construction of a field-aligned parametrization, suitable simplifications and their consequences need to be investigated.

Availability of code

The demonstration code for homogenization-based topology optimization can be accessed through https://github.com/Junpeng-Wang-TUM/TopRank3.

CRediT authorship contribution statement

Junpeng Wang: Writing – original draft, Software, Methodology, Conceptualization. **Rüdiger Westermann:** Writing – review & editing, Supervision, Methodology, Funding acquisition, Conceptualization. **Xifeng Gao:** Writing – review & editing, Methodology. **Jun Wu:** Writing – review & editing, Supervision, Methodology, Conceptualization.

Declaration of competing interest

The authors declare that they have no known competing financial interests or personal relationships that could have appeared to influence the work reported in this paper.

Data availability

No data was used for the research described in the article.

Acknowledgments

We thank Peter Dørffler Ladegaard Jensen from the Technical University of Denmark for the helpful discussion. This work was supported in part by a grant from German Research Foundation (DFG) under grant number WE 2754/10-1.

Appendix. Elasticity tensor of rank-3

In a variety of related works [22,24,25], the general description of the elasticity tensor ($\boldsymbol{S}$) of rank-3 is given as below

$$S_{ijkl} = S^{+}_{ijkl} - (1-\rho)\left[(S^{+}_{ijkl} - S^{-}_{ijkl})^{-1} - \frac{\rho(1-\upsilon_0^2)}{E^{+}}\left(\sum_{n=1}^{3} P_n \Lambda^{n}_{ijkl}\right)\right]^{-1} \tag{15}$$

Here, same as the elasticity tensor of the plane problem, S_{ijkl} is a fourth-order tensor. S^{+}_{ijkl} and S^{-}_{ijkl} are the elasticity tensors of the isotropic solid and 'void' materials and are given by Hooke's law

$$\begin{bmatrix} S^{+/-}_{1111} & S^{+/-}_{1122} & S^{+/-}_{1112} \\ & S^{+/-}_{2222} & S^{+/-}_{2212} \\ sym & & S^{+/-}_{1212} \end{bmatrix} = \frac{E^{+/-}}{1-\upsilon_0^2}\begin{bmatrix} 1 & \upsilon & 0 \\ & 1 & 0 \\ sym & & 2(1-\upsilon_0) \end{bmatrix} \tag{16}$$

E^{+} and υ_0 are Young's modulus and Poisson's ratio of the isotropic solid material. $P_n > 0$ depicts the relative contribution of layer n to the stiffness, which subjects to $\sum_{n=1}^{3} P_n = 1$, and $P_n = \frac{\rho_n}{\rho}$. Combining P_n and Λ^{n}_{ijkl}, the item $\sum_{n=1}^{3} P_n \Lambda^{n}_{ijkl}$ parametrizes all of the possible properties of rank-3 laminate in the entire design space with a fixed volume fraction. Λ is defined as

$$\Lambda^{n}_{ijkl} = n^n_i n^n_j n^n_k n^n_l + \frac{t^n_i n^n_j t^n_k n^n_l + n^n_i t^n_j t^n_k n^n_l + t^n_i n^n_j n^n_k t^n_l + n^n_i t^n_j n^n_k t^n_l}{2\left(1-\upsilon_0\right)} \tag{17}$$

Here, $\boldsymbol{n}^n$ and $\boldsymbol{t}^n$ are the components of normal and tangent of layer n. Let $\boldsymbol{n}^n = [\cos\theta_n \ \sin\theta_n]$ and $\boldsymbol{t}^n = [-\sin\theta_n \ \cos\theta_n]$, here θ_n is the orientation angle of the normal of layer n to the x-axis in a standard coordinate system, all the components of Λ^{n}_{ijkl} are respectively expressed by

$$\begin{aligned}
&\Lambda^n_{1111} = \tfrac{\cos(4\theta_n)+4\cos(2\theta_n)+3}{8} + \tfrac{1-\cos(4\theta_n)}{4(1-\upsilon_0)};\\
&\Lambda^n_{2222} = \tfrac{\cos(4\theta_n)-4\cos(2\theta_n)+3}{8} + \tfrac{1-\cos(4\theta_n)}{4(1-\upsilon_0)};\\
&\Lambda^n_{1122} = \Lambda^n_{2211} = \tfrac{1-\cos(4\theta_n)}{8} - \tfrac{1-\cos(4\theta_n)}{4(1-\upsilon_0)};\\
&\Lambda^n_{1112} = \Lambda^n_{1121} = \Lambda^n_{2111} = \tfrac{2\sin(2\theta_n)+\sin(4\theta_n)}{8} - \tfrac{\sin(4\theta_n)}{4(1-\upsilon_0)};\\
&\Lambda^n_{1222} = \Lambda^n_{2221} = \Lambda^n_{2122} = \Lambda^n_{2212} = \tfrac{2\sin(2\theta_n)-\sin(4\theta_n)}{8} + \tfrac{\sin(4\theta_n)}{4(1-\upsilon_0)};\\
&\Lambda^n_{1212} = \Lambda^n_{1221} = \Lambda^n_{2112} = \Lambda^n_{2121} = \tfrac{1-\cos(4\theta_n)}{8} + \tfrac{1+\cos(4\theta_n)}{4(1-\upsilon_0)}.
\end{aligned} \tag{18}$$

In practical computation, Eq. (15) is usually given in a convenient matrix form [24]

$$\boldsymbol{S}^{[2]} = \boldsymbol{S}^{+} - (1-\rho)\left[(\boldsymbol{S}^{+} - \boldsymbol{S}^{-})^{-1} - \frac{\rho(1-\upsilon_0^2)}{E^{+}}\mathcal{M}\right]^{-1} \tag{19}$$

Here, $\mathcal{M} = \sum_{n=1}^{3} P_n \boldsymbol{\Lambda}^n$, and the matrices $\boldsymbol{S}^{+}$, $\boldsymbol{S}^{-}$ and $\boldsymbol{\Lambda}^n$ are obtained from the corresponding fourth-order tensor components through the transformation below

$$\boldsymbol{A} = \begin{bmatrix} \frac{1}{2}(A_{1111} + A_{2222}) - A_{1122} & A_{1112} - A_{2221} & \frac{1}{2}(A_{1111} - A_{2222}) \\ & 2A_{1212} & A_{1112} + A_{2221} \\ sym & & \frac{1}{2}(A_{1111} + A_{2222}) + A_{1122} \end{bmatrix} \tag{20}$$

Let

$$\begin{aligned}
m_1 &= \sum_{n=1}^{3} p_n \cos(2\theta_n), \quad m_2 = \sum_{n=1}^{3} p_n \sin(2\theta_n),\\
m_3 &= \sum_{n=1}^{3} p_n \cos(4\theta_n), \quad m_4 = \sum_{n=1}^{3} p_n \sin(4\theta_n).
\end{aligned} \tag{21}$$

Then, the matrix $\mathcal{M}$ is rearranged into a simpler form

$$\mathcal{M} = \begin{bmatrix} \frac{3-\upsilon_0-(1+\upsilon_0)m_3}{4(1-\upsilon_0)} & -\frac{(1+\upsilon_0)m_4}{4(1-\upsilon_0)} & \frac{m_1}{2} \\ & \frac{3-\upsilon_0+(1+\upsilon_0)m_3}{4(1-\upsilon_0)} & \frac{m_2}{2} \\ sym & & \frac{1}{2} \end{bmatrix} \tag{22}$$

Upon obtaining $\boldsymbol{S}$, one can get the components of S_{ijkl} in the following way

$$\boldsymbol{S} = \begin{bmatrix} S_{1111} & S_{1122} & S_{1112} \\ & S_{2222} & S_{2221} \\ sym & & S_{1212} \end{bmatrix} = \begin{bmatrix} \frac{1}{2}(S^{[2]}_{11} + S^{[2]}_{33}) + S^{[2]}_{13} & -\frac{1}{2}(S^{[2]}_{11} - S^{[2]}_{33}) & \frac{1}{2}(S^{[2]}_{12} + S^{[2]}_{23}) \\ & \frac{1}{2}(S^{[2]}_{11} + S^{[2]}_{33}) - S^{[2]}_{13} & -\frac{1}{2}(S^{[2]}_{12} - S^{[2]}_{23}) \\ sym & & \frac{1}{2}S^{[2]}_{22} \end{bmatrix} \tag{23}$$

For details of the derivation process above, we refer to [24].

References

[1] Ajit Panesar, Meisam Abdi, Duncan Hickman, Ian Ashcroft, Strategies for functionally graded lattice structures derived using topology optimisation for Additive Manufacturing, Addit. Manuf. 19 (2018) 81–94, http://dx.doi.org/10.1016/j.addma.2017.11.008.

[2] Anders Clausen, Niels Aage, Ole Sigmund, Exploiting additive manufacturing infill in topology optimization for improved buckling load, Engineering 2 (2) (2016) 250–257, http://dx.doi.org/10.1016/J.ENG.2016.02.006.

[3] Jun Wu, Niels Aage, Rüdiger Westermann, Ole Sigmund, Infill optimization for additive manufacturing – approaching bone-like porous structures, IEEE Trans. Vis. Comput. Graphics 24 (2) (2018) 1127–1140, http://dx.doi.org/10.1109/TVCG.2017.2655523.

[4] Jun Wu, Ole Sigmund, Jeroen P. Groen, Topology optimization of multi-scale structures: a review, Struct. Multidiscip. Optim. (2021) 1–26, http://dx.doi.org/10.1007/s00158-021-02881-8.

[5] Pauli Pedersen, On optimal orientation of orthotropic materials, Struct. Optim. 1 (2) (1989) 101–106, http://dx.doi.org/10.1007/BF01637666.

[6] Tsz-Ho Kwok, Yongqiang Li, Yong Chen, A structural topology design method based on principal stress line, Comput. Aided Des. 80 (2016) 19–31, http://dx.doi.org/10.1016/j.cad.2016.07.005.

[7] Stephen Daynes, Stefanie Feih, Wen Feng Lu, Jun Wei, Optimisation of functionally graded lattice structures using isostatic lines, Mater. Des. 127 (2017) 215–223, http://dx.doi.org/10.1016/j.matdes.2017.04.082.

[8] O. Pantz, K. Trabelsi, A post-treatment of the homogenization method for shape optimization, SIAM J. Control Optim. 47 (3) (2008) 1380–1398, http://dx.doi.org/10.1137/070688900.

[9] Jeroen P. Groen, Ole Sigmund, Homogenization-based topology optimization for high-resolution manufacturable microstructures, Internat. J. Numer. Methods Engrg. 113 (8) (2018) 1148–1163, http://dx.doi.org/10.1002/nme.5575.

[10] Jun Wu, Weiming Wang, Xifeng Gao, Design and optimization of conforming lattice structures, IEEE Trans. Vis. Comput. Graphics 27 (1) (2021) 43–56, http://dx.doi.org/10.1109/TVCG.2019.2938946.

[11] Martin Philip Bendsøe, Noboru Kikuchi, Generating optimal topologies in structural design using a homogenization method, Comput. Methods Appl. Mech. Engrg. 71 (2) (1988) 197–224, http://dx.doi.org/10.1016/0045-7825(88)90086-2.

[12] Yuming Huang, Guoxin Fang, Tianyu Zhang, Charlie C.L. Wang, Turning-angle optimized printing path of continuous carbon fiber for cellular structures, Addit. Manuf. 68 (2023) 103501, http://dx.doi.org/10.1016/j.addma.2023.103501.

[13] Junpeng Wang, Rüdiger Westermann, Jun Wu, A streamline-guided dehomogenization approach for structural design, J. Mech. Des. 145 (2) (2023) 021702, http://dx.doi.org/10.1115/1.4056148.

[14] Grégoire Allaire, Perle Geoffroy-Donders, Olivier Pantz, Topology optimization of modulated and oriented periodic microstructures by the homogenization method, Comput. Math. Appl. 78 (7) (2019) 2197–2229, http://dx.doi.org/10.1016/j.camwa.2018.08.007.

[15] Jeroen P. Groen, Jun Wu, Ole Sigmund, Homogenization-based stiffness optimization and projection of 2D coated structures with orthotropic infill, Comput. Methods Appl. Mech. Engrg. 349 (2019) 722–742, http://dx.doi.org/10.1016/j.cma.2019.02.031.

[16] Jeroen P. Groen, Florian C. Stutz, Niels Aage, Jakob A. Bærentzen, Ole Sigmund, De-homogenization of optimal multi-scale 3D topologies, Comput. Methods Appl. Mech. Engrg. 364 (2020) 112979, http://dx.doi.org/10.1016/j.cma.2020.112979.

[17] Perle Geoffroy-Donders, Grégoire Allaire, Olivier Pantz, 3-d topology optimization of modulated and oriented periodic microstructures by the homogenization method, J. Comput. Phys. 401 (2020) 108994, http://dx.doi.org/10.1016/j.jcp.2019.108994.

[18] Florian Cyril Stutz, Tim Felle Olsen, Jeroen Peter Groen, Niels Aage, Ole Sigmund, Justin Solomon, Jakob Andreas Bærentzen, Synthesis of frame field-aligned multi-laminar structures, ACM Trans. Graph. (2022) http://dx.doi.org/10.1145/3516522.

[19] Martin Ohrt Elingaard, Niels Aage, Jakob Andreas Bærentzen, Ole Sigmund, De-homogenization using convolutional neural networks, Comput. Methods Appl. Mech. Engrg. 388 (2022) 114197, http://dx.doi.org/10.1016/j.cma.2021.114197.

[20] Rebekka V. Woldseth, J. Andreas Bærentzen, Ole Sigmund, Phasor noise for dehomogenisation in 2D multiscale topology optimisation, Comput. Methods Appl. Mech. Engrg. 418 (2024) 116551, http://dx.doi.org/10.1016/j.cma.2023.116551.

[21] F.C. Stutz, J.P. Groen, O. Sigmund, J.A. Bærentzen, Singularity aware de-homogenization for high-resolution topology optimized structures, Struct. Multidiscip. Optim. (2020) http://dx.doi.org/10.1007/s00158-020-02681-6.

[22] Peter Dørffler Ladegaard Jensen, Ole Sigmund, Jeroen P. Groen, De-homogenization of optimal 2D topologies for multiple loading cases, Comput. Methods Appl. Mech. Engrg. 399 (2022) 115426, http://dx.doi.org/10.1016/j.cma.2022.115426.

[23] Wenzel Jakob, Marco Tarini, Daniele Panozzo, Olga Sorkine-Hornung, et al., Instant field-aligned meshes, ACM Trans. Graph. 34 (6) (2015) 1–15, http://dx.doi.org/10.1145/2816795.2818078.

[24] L.A. Krog, Niels Olhoff, Topology and Reinforcement Layout Optimization of Disk, Plate, and Shell Structures, Springer, 1997, http://dx.doi.org/10.1007/978-3-7091-2566-3_9.

[25] Jeroen Peter Groen, Multi-Scale Design Methods for Topology Optimization, DTU Mechanical Engineering, 2018.

[26] B. Hassani, E. Hinton, A review of homogenization and topology optimization I—homogenization theory for media with periodic structure, Comput. Struct. 69 (6) (1998) 707–717, http://dx.doi.org/10.1016/S0045-7949(98)00131-X.

[27] Martin P. Bendsøe, Optimization of Structural Topology, Shape, and Material, vol. 414, Springer, 1995, http://dx.doi.org/10.1007/978-3-662-03115-5.

[28] Krister Svanberg, The method of moving asymptotes—a new method for structural optimization, Internat. J. Numer. Methods Engrg. 24 (2) (1987) 359–373, http://dx.doi.org/10.1002/nme.1620240207.

[29] Blaise Bourdin, Filters in topology optimization, Internat. J. Numer. Methods Engrg. 50 (9) (2001) 2143–2158, http://dx.doi.org/10.1002/nme.116.

[30] Fengwen Wang, Boyan Stefanov Lazarov, Ole Sigmund, On projection methods, convergence and robust formulations in topology optimization, Struct. Multidiscip. Optim. 43 (6) (2011) 767–784, http://dx.doi.org/10.1007/s00158-010-0602-y.

[31] Junpeng Wang, Jun Wu, Rüdiger Westermann, Stress topology analysis for porous infill optimization, Struct. Multidiscip. Optim. 65 (3) (2022) 1–13, http://dx.doi.org/10.1007/s00158-022-03186-0.

[32] Junpeng Wang, Jun Wu, Rüdiger Westermann, Stress trajectory guided structural design and topology optimization, in: International Design Engineering Technical Conferences and Computers and Information in Engineering Conference, Vol. 1, American Society of Mechanical Engineers, 2022, p. 1, http://dx.doi.org/10.1115/DETC2022-89030.

[33] Erik Träff, Ole Sigmund, J.P. Groen, Simple single-scale microstructures based on optimal rank-3 laminates, Struct. Multidiscip. Optim. 59 (4) (2019) 1021–1031, http://dx.doi.org/10.1007/s00158-018-2180-3.

[34] Jonathan Palacios, Eugene Zhang, Rotational symmetry field design on surfaces, ACM Trans. Graph. 26 (3) (2007) 55–es, http://dx.doi.org/10.1145/1276377.1276446.

[35] Nicolas Ray, Bruno Vallet, Wan Chiu Li, Bruno Lévy, N-symmetry direction field design, ACM Trans. Graph. 27 (2) (2008) 1–13, http://dx.doi.org/10.1145/1356682.1356683.

[36] Hui Liu, Lianxiong Chen, Yi Jiang, Dezhou Zhu, Yufa Zhou, Xinzhong Wang, Multiscale optimization of additively manufactured graded non-stochastic and stochastic lattice structures, Compos. Struct. 305 (2023) 116546, http://dx.doi.org/10.1016/j.compstruct.2022.116546.

[37] Gilles Francfort, Franc Murat, Luc Tartar, et al., Fourth order moments of nonnegative measures on S^2 and applications, Arch. Ration. Mech. Anal. 131 (1995) 305–333, http://dx.doi.org/10.1007/BF00380913.

[38] Alejandro R. Diaz, Robert Lipton, Optimal material layout in three-dimensional elastic structures subjected to multiple loads, Mech. Struct. Mach. 28 (2000) 219–236, http://dx.doi.org/10.1081/SME-100100619.